Nuclear Science and Techniques (2025) 36:166
https://doi.org/10.1007/s41365-025-01740-1

Layered reconstruction framework for longitudinal segmented electromagnetic calorimeter

Jia-Le Fei[1] · Ao Yuan[1] · Ke Wei[2] · Liang Sun[2] · Ji-Ke Wang[1]

Received: 29 October 2024 / Revised: 24 December 2024 / Accepted: 1 January 2025 / Published online: 28 June 2025

Abstract
In future high-energy physics experiments, the electromagnetic calorimeter (ECAL) should operate with an exceptionally high luminosity. An ECAL featuring a layered readout in the longitudinal direction and precise time-stamped information offers a multidimensional view, thereby enriching our understanding of the showering process of electromagnetic particles in high-luminosity environments. This was used as the baseline design for several new experiments, including the planned upgrades of the current running experiments. Reconstructing and matching multidimensional information across different layers poses new challenges for the effective utilization of layered data. This study introduced a novel layered reconstruction framework for ECAL with a layered readout information structure and developed a corresponding layered clustering algorithm. This expands the concept of clusters from a plane to multiple layers. Additionally, this study presents the corresponding layered cluster correction methods, investigates the transverse shower profile utilized for overlapping cluster splitting, and develops a layered merged π^0 reconstruction algorithm based on this framework. By incorporating energy and time information into 3-dimensions, this framework provides a suitable software platform for preliminary research on longitudinally segmented ECAL and new perspectives in physics analyses. Furthermore, using the PicoCal in LHCb Upgrade II as a concrete example, the performance of the framework was preliminarily evaluated using single photons and π^0 particles from the neutral B^0 meson decay $B^0 \to \pi^+\pi^-\pi^0$ as benchmarks. The results demonstrate that, compared to the unlayered framework, utilizing this framework for longitudinally segmented ECAL significantly enhances the position resolution and the ability to split overlapping clusters, thereby improving the reconstruction resolution and efficiency for photons and π^0s.

Keywords Electromagnetic calorimeter · Layered reconstruction · Transverse shower profile · Merged π^0 reconstruction

1 Introduction

An electromagnetic calorimeter (ECAL) is a detector used to measure the energy and momentum of high-energy electromagnetic particles (e.g., electrons and photons). In particle physics, ECALs can measure the electromagnetic showering of particles within it and determine the energy and momentum of electromagnetic particles based on energy deposition, providing important information for understanding the properties and interactions of elementary particles.

A high-performance ECAL is crucial for the precise detection of high-energy physical phenomena and has been validated in many experiments [1–4]. For instance, in the context of the LHCb experiment, during Runs 1 and 2 of the Large Hadron Collider (LHC), approximately 33% of the decay products of heavy-flavor particles are neutral particles, which decay into photons, such as π^0 [5]. These photons exhibit a broad energy spectrum, ranging from a few gigaelectronvolts to several hundred gigaelectronvolts [6]. Owing to the outstanding performance of ECAL in the LHCb [7, 8], Runs 1 and 2 yielded many impactful studies involving photons, π^0s, and electrons. This research explored photon polarization in the $b \to s\gamma$ process [9], radiative B_s^0 decay [10], and other related studies. In addition, quantification of CP violations in decays, such as

✉ Liang Sun
liang.sun@cern.ch

✉ Ji-Ke Wang
jike.wang@cern.ch

[1] The Institute for Advanced Studies, Wuhan University, Wuhan 430072, China

[2] School of Physics and Technology, Wuhan University, Wuhan 430072, China

$B^+ \to K^+\pi^0$ [11] and $D^0 \to \pi^+\pi^-\pi^0$ decays[12], was conducted. Furthermore, intriguing investigations into lepton universality through the reconstruction of $b \to s\ell^+\ell^-$ transitions have been conducted [13, 14]. This research also includes rare decay searches, such as $B_s^0 \to \mu^+\mu^-\gamma$ [15].

In pursuit of new physics at the LHC, a high-luminosity LHC (HL-LHC) project was proposed to enhance the accumulation of collision data within a shorter timeframe [16–18]. Operating with an instantaneous luminosity of 10^{34} cm^{-2}s^{-1}, the HL-LHC aims to achieve impressive integrated luminosity over its operational lifetime [17, 19]. However, such a high-luminosity environment presents challenges, such as increased detector occupancy, vertex pile-ups, and radiation resistance concerns. Many current detectors at the LHC are no longer adequate for operation under HL-LHC conditions, and long-term radiation damage necessitates urgent replacements. To ensure optimal detector performance in high-luminosity environments and enable exploration of new physics, several experiments are planning detector upgrades [20–24].

The showering process of electromagnetic particles in an ECAL is influenced by factors such as particle type and incident energy, which in turn affect the distribution of the deposited energy [25]. An ECAL equipped with multiple readout channels spanning both the transverse and longitudinal directions facilitates the capture of time, energy, and other readout data in dual dimensions. This capability significantly enhances our comprehensive understanding of the physical processes within the ECAL across multiple dimensions, ultimately leading to improved accuracy in reconstructing the energy and momentum of the particles. Therefore, a longitudinally segmented ECAL has been considered a baseline design for upgrades in many experiments.

The development of event reconstruction algorithms that fully exploit the energy, position, and time information acquired from longitudinally segmented ECAL will enhance the precision of energy-momentum reconstruction, cluster splitting, and particle identification, thereby facilitating the achievement of defined physical objectives. However, this also introduces new challenges in the reconstruction, matching, and efficient utilization of longitudinal-layer information. To leverage the advantages of layered readouts in forthcoming high-energy physics experiments, such as CMS and ALICE [26–31], diverse software frameworks and reconstruction algorithms have been devised and customized to effectively utilize and store layered information.

Building on this background, this study presents a comprehensive software framework tailored for a longitudinally segmented ECAL, along with the development of a layered clustering algorithm and cluster correction workflow. The layered reconstruction framework outlined in this study merges data from all the layers to identify potential Cluster^{3D} candidates. Subsequently, a seed is identified in each layer from the readout cells of the Cluster^{3D} candidates. Utilizing these seeds as focal points, Cluster^{2D}s in all readout layers are reconstructed (the definitions of Cluster^{3D} and Cluster^{2D} are elaborated on in subsequent sections). Finally, the performance is compared with that of an unlayered-reconstruction algorithm that combines the information from the corresponding readout units in each layer based on the single-photon resolution, as well as the reconstruction resolution and efficiency for π^0 from $B^0 \to \pi^+\pi^-\pi^0$. This comparison leveraged the 2023 baseline setup of ECAL in the LHCb Upgrade II (PicoCal) [32, 33].

2 Software framework and data structures

The layered reconstruction framework is shown in Fig. 1. The modeling of the detector geometry is the cornerstone of the framework. To adapt as many longitudinally segmented ECAL structures as possible, the following data structures were constructed to describe and carry the geometrical information of the ECAL in this framework.

Calorimeter: It represents the ECAL and also stores the absolute coordinates and size of the entire ECAL in space.
Region: It is a virtual geometry containing a series of modules with identical detector structure, material, and installation angle. It was used to store the calibration and cluster correction parameters for this series of modules.
Module: It represents the minimum installation unit and stores the absolute coordinates, size and installation angle of itself.
Layer: It is the key geometric data structure in this framework and physically represents a longitudinal segment of the module. It stores all Cell^{2D}s located in a segmented readout layer in a module.
Cell^{2D}: It represents the minimum readout channels in modules and contains information regarding the mounting position of the readout cell, signal, and timestamp.

Based on the aforementioned basic geometric structure, the following cluster data structures, containing two or more Cell^{2D}s, were constructed, which correspond to the cluster layer in the software framework. The specific construction method for the data structures is described in Sect. 3.1.

Cell^{3D} It consists of multiple Cell^{2D}s in the longitudinal direction.

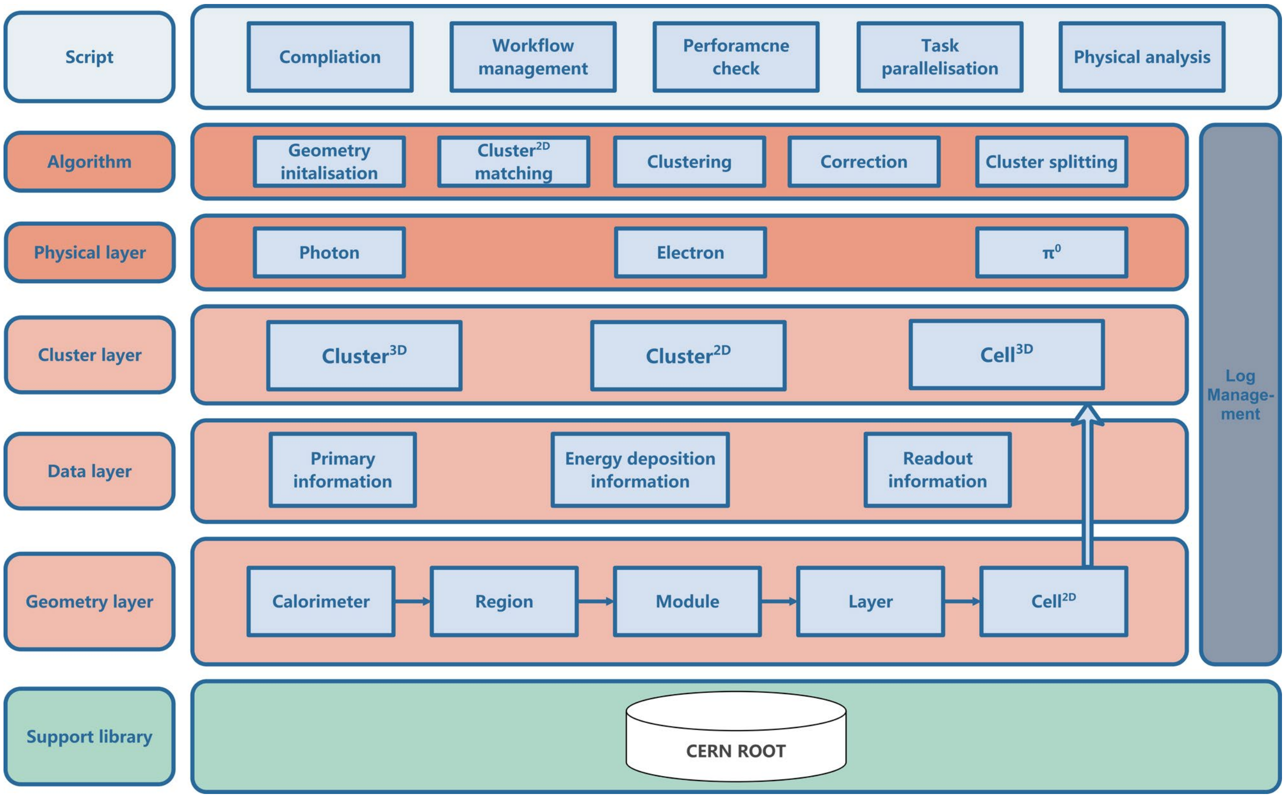

Fig. 1 Software framework

Cluster^{2D} It consists of multiple Cell^{2D}s at the same layer.

Cluster^{3D} It consists of a Cluster^{2D} and multiple Cell^{2D}s in each layer and would be considered as a candidate for photons, electrons, or merged π^0s.

3 Reconstruction

Based on the layered reconstruction framework, this section describes the reconstruction algorithm for Cluster^{3D}, which is a candidate for electromagnetic particles (γ/e). The methodology for reconstructing a merged π^0 by splitting a single Cluster^{3D} is also discussed. In addition, it outlines the process for correcting various parameters of Cluster^{3D}, including the energy, position, and time.

3.1 Layered clustering

The algorithm outlined in this section details the methodology used to finalize the construction of Cluster^{3D}s and provides particle reconstruction information at each readout layer in the form of Cluster^{2D}s. A flowchart of the layered clustering algorithm is shown in Fig. 2d. First, the algorithm searches for Seed^{3D}s on a single layer, which includes a realistic readout layer with a smaller transverse showering width, as well as a virtual single-layer calorimeter constructed by merging information from all readout layers and constructing temporary Cluster^{3D}s in the virtual single-layer calorimeter from Seed^{3D}s. This approach was motivated by two primary considerations.

The first and most important point is that constructing Cluster^{2D} in each layer and performing layer-by-layer matching consumes a significant amount of computation time. First, performing 2-dimensional clustering in a single layer ensures efficient online triggering.

Second, in layers with narrower transverse cluster development, there is a chance of discovering more non-overlapping clusters. However, owing to the narrower transverse cluster development, the energy deposition is lower. Owing to sampling fluctuations, some particles may not have formed effective seeds in this layer. Therefore, searching for Seed^{3D}s in both Cell^{3D}s and Cell^{2D}s in layers with narrower cluster development will help achieve a balance between cluster separation and reconstruction efficiency.

Subsequently, based on the temporary Cluster^{3D}s, we construct Cluster^{2D}s located in different layers to obtain

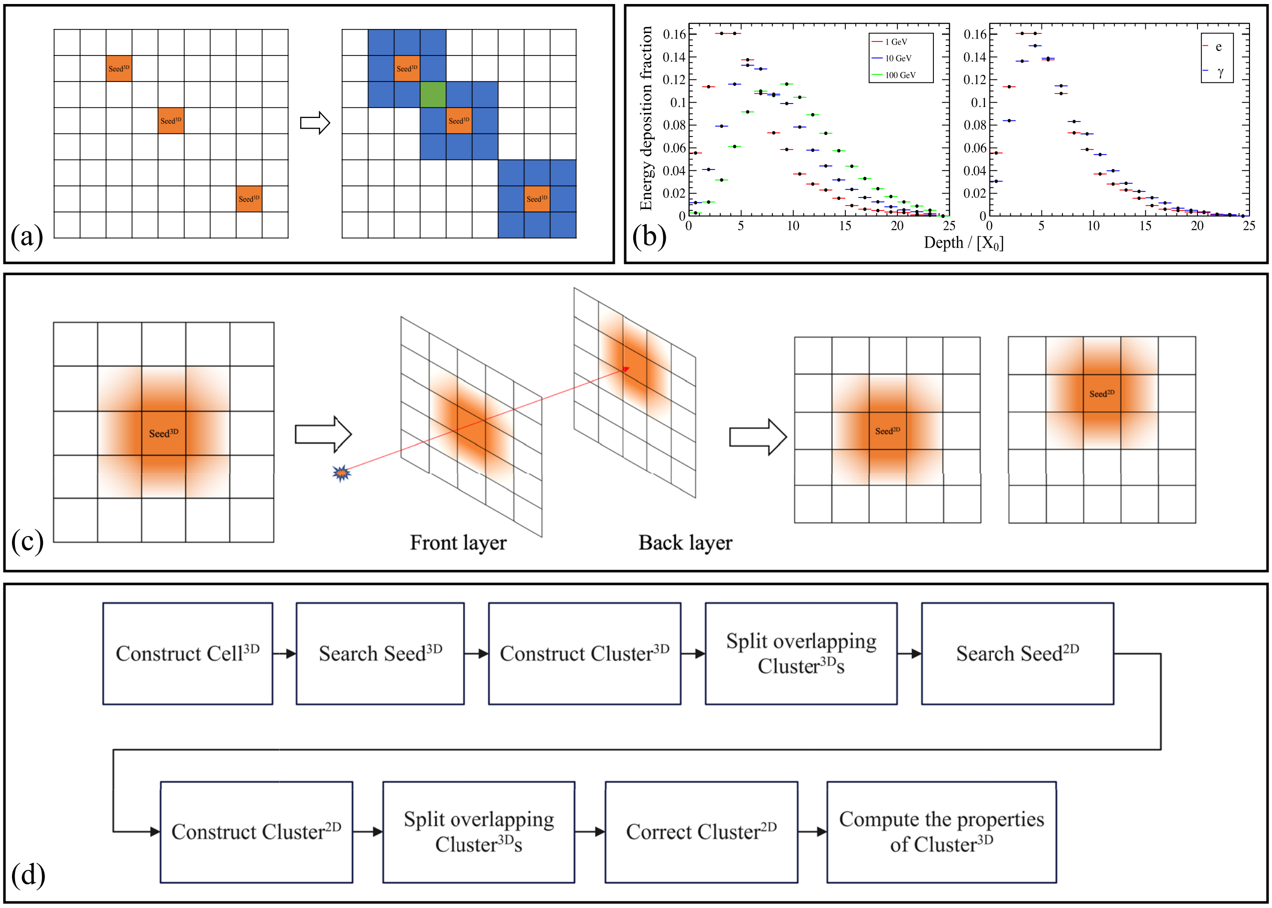

Fig. 2 (Color online) **a** Searching Seed^{3D}s and constructing temporary Cluster^{3D}s centered on Seed^{3D}s, where the orange boxes represent Seed^{3D}s, blue boxes represent Cell^{3D}s, and green box represents Cell^{3D} shared by two Cluster^{3D}s. **b** The energy deposition in the longitudinal direction of ECAL, where the left plot shows electrons with different energies and the right plot shows the electron and photon with 1 GeV energy. **c** Searching for Seed^{2D} in the Cell^{2D} of the temporary Cluster^{3D} and constructing new Cluster^{2D} in each layer. **d** Workflow chart for layered reconstruction

the final Cluster^{3D}s. Information from different layers was initially integrated by constructing a Cell^{3D}. The details of each step of the layered clustering algorithm are as follows:

3.1.1 Constructing Cell^{3D}

To integrate the information in each readout layer, the information from the corresponding Cell^{2D}s in both layers is utilized to establish a novel data structure known as Cell^{3D}. Specifically, Cell^{3D}s were systematically constructed across the transverse section of the ECAL, with a radius equivalent to the module's Molière radius. Along the longitudinal direction of the ECAL, all Cell^{2D}s falling within the transverse span of Cell^{3D} are amalgamated into Cell^{3D}, with each Cell^{2D} being included only once. The energy of Cell^{3D} is determined by the cumulative energy of the Cell^{2D}s it encompasses, and the position of Cell^{3D} is defined as its geometric center.

3.1.2 Searching Seed^{3D} and constructing temporary Cluster^{3D}

When an electromagnetic particle strikes the ECAL, it radiates energy outward from the impact point, typically resulting in the formation of Cell^{2D} and Cell^{3D} with the highest local energy deposition near the impact point. Therefore, as illustrated in Fig. 2a, the initial step in clustering is to iterate through all Cell^{3D}s and Cell^{2D}s in specific layers to identify the Cell^{3D} and Cell^{2D} layers that exhibit the highest local energy deposition. For the local maximum Cell^{2D}, the corresponding Cell^{3D} is considered a Seed^{3D}. Simultaneously, the local maximum Cell^{3D} is considered as Seed^{3D}. *seed* denotes the initial step in the clustering process.

To prevent faker Seed^{3D}s during the seeding process, all identified Seed^{3D} s must satisfy a transverse momentum cut, typically defined as greater than 50 MeV in this framework. The threshold value of this cut can be lowered if required to investigate phenomena related to soft photons or electrons. All Seed^{3D}s passing through the cut are labeled as final Seed^{3D}s and stored.

As a result of transverse particle showering, the energy is not fully contained within Seed^{3D}. Hence, it is imperative to encompass a specific range of Cell^{3D}s around Seed^{3D} to guarantee optimal coverage of all energy deposits from the particles. In this study, we followed the methods described in Ref. [34], which uses a fixed-size window to incorporate Cell^{3D}s. The specific procedure is as follows: Centered around the Seed^{3D}s, the Cluster^{3D}s are formed by incorporating all Cell^{3D}s within a 3×3 window around the Seed^{3D}s, as illustrated in Fig. 2a. Additionally, the Cell^{2D}s from all layers encompassed by the Cell^{3D}s are also included as members of the Cluster^{3D}s. However, when the Seed^{3D} s are located at the boundary of the region, special treatment is required because of the different types of Cell^{3D}s in different regions. Around Seed^{3D}, within a radius of 1.5 times the size of Seed^{3D}, Cell^{3D}s belonging to other regions are also included. In this study, a detailed description of the process is not provided. This process may lead to Cluster^{3D} at the boundary containing several Cell^{3D}s, which may be greater or less than nine, and its shape may be irregular. This requires separate handling of Cluster^{3D} at the boundary in the Cluster^{3D} correction process described later.

In the subsequent steps, further layered modifications were made to the Cell^{2D}s included in Cluster^{3D}. Therefore, Cluster^{3D} obtained in this section is referred to as a temporary Cluster^{3D}.

3.1.3 Searching Seed^{2D} and reconstructing Cluster^{2D}

Because of the incident angle of the particles and the rotation of certain modules, as the shower evolves longitudinally, the energy centroid of the shower varies across different layers. This results in Cell^{2D} with the highest local energy in each layer, not always being encompassed within Seed^{3D}, as shown in Fig. 2c.

To identify the Seed^{2D} in each layer, we iterate through the Cell^{2D}s of each layer in the temporary Cluster^{3D} and select the Cell^{2D} with the highest energy as the Seed^{2D} of that layer. Moreover, the overlap of Cluster^{2D}s results in an increased accumulation of energy in shared Cell^{2D}s, which may cause the energy of a shared Cell^{2D} to exceed that of a Seed^{2D}, leading to the misidentification of a shared Cell^{2D} as a Seed^{2D}. Therefore, before searching for Seed^{2D}, energy splitting must be performed on all overlapping Cluster^{2D}s, as shown in Fig. 2d, and is discussed in detail in Sect. 3.2.3.

Subsequently, Cluster^{2D}s are formed with Seed^{2D}s as the center, and all Cell^{2D}s within the Molière radius of the module centered on Seed^{2D}s in the same layer are included in the Cluster^{2D}s. The raw energy, position, and timestamp of the Cluster^{2D}s were computed using the following equations:

$$\begin{aligned} E_{\text{raw}} &= \sum_{i=1}^{n} E_i, \\ r_{\text{raw}} &= \frac{\sum_{i=1}^{n} E_i \times r_i}{E_{\text{raw}}}; \quad r = x \text{ or } y, \\ t_{\text{raw}} &= t_{\text{Seed}^{2D}}, \end{aligned} \tag{1}$$

where n represents the number of Cell^{2D}s in Cluster^{2D}, and r_i and E_i represent the position and energy of Cell^{2D}s, respectively.

Finally, a new Cluster^{3D} containing Cluster^{2D}s in all layers is constructed. The raw energy of Cluster^{3D} is computed using the following formula:

$$E_{\text{raw}}^{3D} = \sum_{i=1}^{n} E_i, \tag{2}$$

where E_i represents the energy of the Cell^{2D}s, and n represents the number of Cell^{2D}s in all the layers incorporated in Cluster^{3D}. As shown in Fig. 2b, the energy deposition distribution of the incident particles depends on their type and energy of the incident particles. Therefore, unreasonable Cluster^{3D}s can be filtered based on the energy ratio of Cluster^{2D}s in each layer. The position information of Cluster^{2D}s is considered as a point of the incident particle momentum direction on the corresponding layer, with the time information serving as the timestamp for this coordinate point. Additionally, the energy information is regarded as the total deposited energy of the particles in that layer. Reconstructing and correcting the information of the particles along the momentum direction layer-by-layer helps improve the position resolution, which will be discussed in detail in Sect. 4.

3.2 Cluster^{3D} correction

The goal of the Cluster^{3D} correction is to reduce the bias between the reconstructed and actual values, while also aiming for the minimal standard deviation of the reconstructed values. In the layered reconstruction framework, the position and timestamp of Cluster^{3D} are calculated and corrected from the Cluster^{2D} level. As described in Sect. 3.1, the raw position and timestamp of Cluster^{2D} can be calculated using information from the Cell^{2D}s in Cluster^{2D}. Subsequently, the raw position and timestamp information of Cluster^{2D} are corrected, and the position and timestamp information of Cluster^{3D} are calculated using the corrected Cluster^{2D}. The energy of Cluster^{3D} was

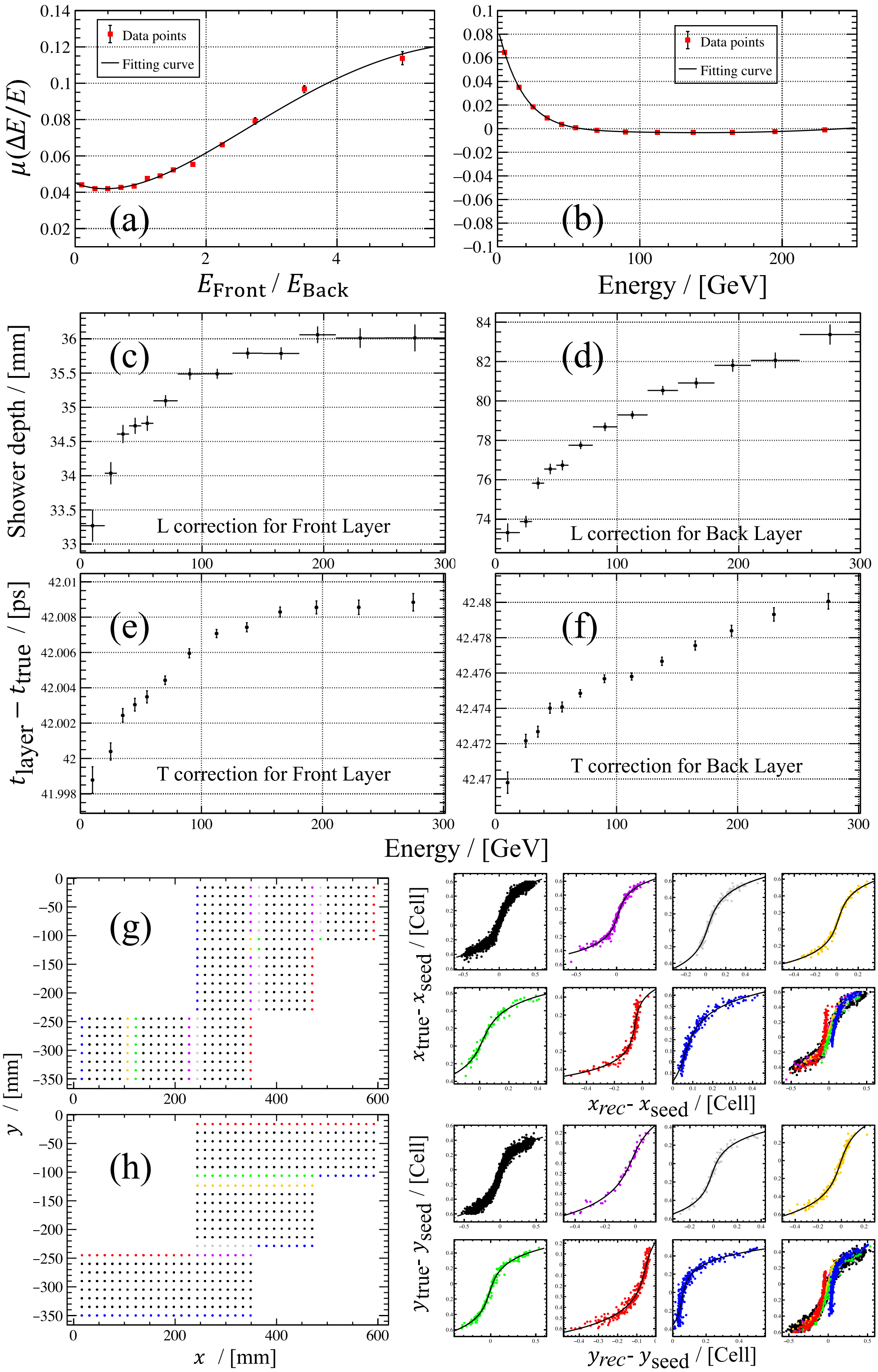

Fig. 3 (Color online) **a**, **b** The energy correction. Here, ΔE is the difference between the true energy and the reconstructed energy, E is the true energy, and μ represents the mean value which is derived from the Gaussian fitting. **c**, **d** The L correction, where the shower depth is measured from the front surface of the ECAL. **e**, **f** The time correction points, where t_{true} is the true time of the particle at the front face of the ECAL. **g**, **h** The S correction

also corrected using the energy ratios of Cluster^{2D}s in different layers. To provide a more detailed illustration of the specifics of layered corrections, Fig. 3 also displays some examples of the longitudinally segmented PicoCal in LHCb Upgrade II, where *Front* and *Back* represent the front and back layers of the abovementioned ECAL.

3.2.1 Energy correction

The objective of energy correction is to correct the energy of Cluster^{3D} to match that of the incident particles. Errors in reconstructing the energy of an incident particle typically stem from the following sources:

Intrinsic error of ECAL readout cell: It comes from the response linearity of sensitive materials, thermal noise in electronic systems, sampling errors in analog to digital converters (ADC), etc.

Calibration error of the readout cell: The shower development in the longitudinal direction is energy related, and the proportion of physical processes dominated in energy deposition changes at different stages of shower development. This leads to changes in the sampling fraction of the ECAL, which ultimately affects the calibration of the readout cell.

Leakage of energy: It is due to the incomplete deposition of particle energy in ECAL and the use of finite-sized windows during clustering.

Fitting error of calibration and correction parameters: It is typically expressed as a constant term in the energy resolution.

In the layered framework of this study, the energy correction of Cluster^{3D}s was divided into two steps, as shown in Fig. 3a and b. The initial correction of the energy of Cluster^{3D} was performed based on the energy ratios of Cluster^{2D}s in different layers. As shown in Fig. 3a, in the example based on PicoCal, we first correct the bias between the reconstructed Cluster^{3D} energy and true energy based on the energy ratio of the front layer to the back layer. Subsequently, as illustrated in Fig. 3b, further correction of the energy of Cluster^{3D}s is conducted based on the total energy of Cluster^{3D}s, which reduces the bias in the low-energy region.

3.2.2 Position and time correction

When a particle passes through the ECAL, it showers and deposits energy along its momentum direction. The center of gravity of the deposited energy in each layer can be considered a point in the direction of the particle momentum. In the layered reconstruction framework, the position of Cluster^{2D} is regarded as the reconstructed position of the center of gravity. Furthermore, Cluster^{2D}s also provide a timestamp, which is related to the hit time of the particle, for the layers to which they belong. For the position and time correction in this study, layered correction is applied to Cluster^{2D}s firstly, followed by the utilization of the corrected information from Cluster^{2D}s to calculate the information of Cluster^{3D}s.

The purpose of position correction is to correct the reconstructed position of Cluster^{2D} as accurately as possible to the center of gravity of the energy deposited by the particles in each layer.

For Cluster^{2D}, the *x*/*y* position information was derived from the energy-weighted positions of the Cell^{2D}s. Based on the model described in Ref. [35], we define Δr_{rec} as the position of Cluster^{2D} minus the position of Seed^{2D}, and Δr_{true} as the position of the true transversal energy barycenter minus the position of Seed^{2D}, in each layer. This study explored the relationship between Δr_{rec} and Δr_{true}. As shown in Fig. 3g and h, the shape of this relationship is like an *S*, so we also call the process of correcting the *x*/*y* coordinates "*S* correction". The shape of *S* is affected by the location of Seed^{2D}. When Seed^{2D} is positioned at the boundaries of the region, the introduction of a varying cell size Cell^{2D} and the presence of installation gaps affect the impact on the *S* shape. This results in a different *S* shape for Cluster^{2D}s located at the boundary of the region compared with those inside the region, as illustrated in Fig. 3g and h.

The *z*-coordinate of the center of gravity of the deposition energy is typically used to evaluate the depth of the shower. Owing to the typically small granularity and thick layers of ECAL in the longitudinal direction, the direct use of the *z*-coordinate information of Cell^{2D} to reconstruct the *z*-coordinate of the gravity center of the deposition energy in each layer introduces substantial uncertainty. Therefore, the reconstruction of the *z*-coordinate is typically performed based on the energies of the incident particles. As shown in Fig. 3c, and d, the shower depth (the difference between the *z*-coordinate of the shower and the *z*-coordinate of the front face of the module) is logarithmically related to the incident particle energy, because the pair production of electrons dominates the energy deposition [36]. This is the rationale behind the term "L correction" for this correction step. By leveraging this correlation, we can deduce the *z*-coordinates of Cluster^{2D} based on the energy of the incoming particles.

For the Cluster^{2D}s, the positions obtained by the above position correction were also projected onto the front surface of ECAL and then used in subsequent steps to calculate the position information of the Cluster^{3D}s.

In this study, the timestamp of the Seed^{2D}s were used as the timestamp for Cluster^{2D}s in the preliminary study. The purpose of time correction is to determine the time difference between the timestamps of Cluster^{2D} in each layer and the moment when the particle reaches a specific

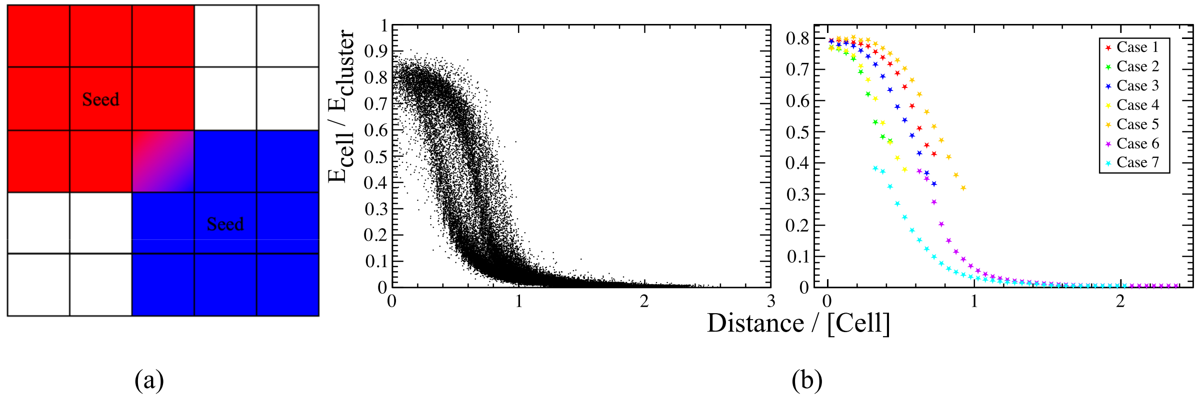

Fig. 4 **a** Two overlapping clusters shared the same cell. **b** The transverse shower profile, where the *y*-axis is the fraction of the energy of the Cell^{2D}s to the energy of the Cluster^{2D}s, and the *x*-axis is the distance between the center of the Cell^{2D}s and the center of the Cluster^{2D}s

reference plane. This time difference is employed to correct the timestamp of Cluster^{2D} to an accurate time on a designated reference plane. The front surface of ECAL was used as the reference plane for time correction in this study. This time difference is related to the energy of the incident particle, and the correction results are shown in Fig. 3e and f. Furthermore, if there is a rotation of the module, it results in a longitudinal positional difference of Cell^{2D}s at different transverse positions in the same layer. This results in a time difference for the particles to reach different Seed^{2D}s on the same layer. Hence, it is necessary to compensate for this time difference based on the longitudinal position difference of Seed^{2D}s as follows:

$$t'_{\mathrm{Seed}^{2D}} = \left(t_{\mathrm{Seed}^{2D}} + \frac{z_{\mathrm{Seed}^{2D}} - z_{\mathrm{layer}}}{v_z} \right), \tag{3}$$

where $t'_{\mathrm{Seed}^{2D}}$ represents the compensated time of Seed^{2D} and v_z represents the velocity of the particle along the direction of the beam pipe.

After obtaining the corrected position and time information of Cluster^{2D}s, the time and position information of Cluster^{3D}s are obtained by weighting the time or position information of Cluster^{2D}s as follows:

$$\begin{aligned} V &= r \text{ or } t, \\ W_i(V) &= \frac{1}{Res_i(V)^2}, \\ V_{\mathrm{Cluster}^{3D}} &= \frac{\sum_{i=1}^{n} (V_{\mathrm{Cluster}_i^{2D}} \times W_i(V))}{\sum_{i=1}^{n} W_i(V)}, \end{aligned} \tag{4}$$

where *r* represents the position, *t* represents the time, *i* represents the number of layers, and Res_i represents the resolution of *r* or *t* in layer *i*, as shown in Fig. 6b and c.

3.2.3 Splitting of overlapping clusters

When two Cluster^{3D}s overlap in an event, as shown in Fig. 4a, it is necessary to conduct energy splitting on the shared Cell^{2D}s to ensure accurate reconstruction of the energy and position of the Cluster^{3D}s. In the layered reconstruction framework, energy splitting of the overlapping Cluster^{3D}s is performed at the Cluster^{2D} level. The general logic of the algorithm is as follows. First, determine if the two Cluster^{3D}s share any Cell^{2D}s. If they do, distribute the energy of the shared Cell^{2D}s between the respective Cluster^{2D}s. Upon completing the energy splitting of Cell^{2D}s, reevaluate the information of Cluster^{2D}s based on the updated energy of Cell^{2D}s, and remake the necessary corrections.

Currently, the energy splitting is determined by the transverse shower profile obtained from MC truth information. This study provides a layered description of the transverse shower profile at the Cell^{2D} level. As shown in Fig. 4b, the transverse shower profile is represented by the distance of Cell^{2D}s from Cluster^{2D}s on the *x*-axis and the energy fraction of Cell^{2D}s relative to Cluster^{2D}s on the *y*-axis.

When Cell^{2D} is shared by two Cluster^{2D}s, the distribution of Cell^{2D} energy to each Cluster^{2D} is evaluated in two steps. First, the energy fraction of the shared Cell^{2D} corresponding to each Cluster^{2D} is calculated based on the distance between Cell^{2D} and Cluster^{2D}, as depicted in Fig. 4b. Second, the estimated energy from each of the two Cluster^{2D}s to Cell^{2D} is computed using the fraction established in the first step and the energy of the Cluster^{2D}s. At this juncture, the total estimated energy from the two Cluster^{2D}s to the shared Cell^{2D} exceeds that of the shared Cell^{2D}. The energy of the shared Cell^{2D} is then distributed between the two Cluster^{2D}s, using the calculated estimated energy as the weighting factor. Subsequently, the energy and position of Cluster^{2D} are recalculated, and the aforementioned procedures are repeated. Upon stabilizing the splitting weights of the shared Cell^{2D} for the two Cluster^{2D}s, this iterative process completes and finalizes the energy splitting of the shared Cell^{2D}.

The precision of the energy fraction contributed by Cell^{2D} to each Cluster^{2D} relies heavily on the accuracy of the transverse shower profile. As depicted in Fig. 4b, even when the distances between Cell^{2D}s and their respective Cluster^{2D}s are identical, the energy contribution from Cell^{2D}s to Cluster^{2D}s can vary significantly and even display multiple peaks, particularly at distances of approximately 0.5 [Cell]. Therefore, it is essential to categorize the data points in the left-hand plot in Fig. 4b to achieve narrower fraction ranges corresponding to the same distance within a single category, as well as a singular peak in the energy fraction.

The classification methods used in this study are listed in Table 1, and the classification results are shown in the right plot of Fig. 4b. First, whether this Cell^{2D} is a Seed^{2D} should be determined. This is because the random scattering direction of the initial electron pairs affects which Cell^{2D} near the hit point has the opportunity to receive more energy. A Cell^{2D} deposited with the maximum energy was constructed as a Seed^{2D} in the reconstruction process. Additionally, because the readout unit (Cell^{2D}) is not circular, the position of the hit point relative to the edges or corners of Seed^{2D} affects the energy fraction of Seed^{2D} when the distance to the hit point remains unchanged. Finally, the position of the hit point and the Cell^{2D}s relative to Seed^{2D} in the positive or negative direction of the particle's transverse momentum also affect the energy fraction, which can be described as being relatively close to or far from the beam pipe in LHCb. In practical operations, the hit position of the particles in each layer is substituted by the position of Cluster^{2D}s.

3.3 Merged π^0 reconstruction

When two photons produced by π^0 cannot be reconstructed individually as two Cluster^{3D}s because of the proximity of the hit points, π^0 is referred to as merged π^0. This section describes the reconstruction of the potential sub-Cluster^{3D} pair, which is considered a candidate for the photon pair from the merged π^0, from a direct reconstruction of Cluster^{3D}. Subsequently, the sub-Cluster^{3D} pair is used to reconstruct the merged π^0. A workflow chart of the merged π^0 reconstruction is presented in Fig. 5b. The following subsection focuses on the algorithms associated with the first and last steps in the workflow chart, which do not appear in single-photon reconstruction.

3.3.1 Searching the second Seed^{2D} in Cluster^{2D}s

During the reconstruction process, a merged π^0 indicates that the generated photon pair was reconstructed as one Cluster^{3D} in ECAL. This indicates that energy deposition from π^0 produces only one local maximum energy Cell^{3D}. For the unlayered-reconstruction framework in some experiments [37, 38] where layered readout information is lacking, it is common practice to select one of the non-seeded cells in the cluster with the highest energy cell as the second seed. A new cluster is then constructed around the second seed as the center. After splitting the energy of the shared cells between the new and original clusters, the overlapping clusters are referred to as subcluster pairs of the original cluster.

As shown in Fig. 5a, a merged π^0 does not necessarily result in "merged" Cluster^{2D} in each layer. According to the cell-energy-splitting algorithm described above, the success rate of splitting increased as the number of cells shared by the two clusters decreased.

Furthermore, it is necessary to base the selection of the second Seed^{2D} on the energy of Cell^{2D}s. This is because the energy of Cell^{2D}s are also related to the distance from the hit point of the photon. When one of the photons resulting from the decay of a π^0 has a much higher energy than the other photon in non-Seed^{2D} Cell^{2D}s, the Cell^{2D} closer to the higher-energy photon may have a higher energy than the Cell^{2D} closest to the lower-energy photon. Solely focusing on the energy of Cell^{2D} may result in misidentifying the second Seed^{2D}.

Hence, motivated by the aforementioned reasons, the layered reconstruction framework described in this study

Table 1 The classification of transverse shower profile

Case	Cell type	Hit position relative to Seed	Cell relative to Seed
1	Seed	1: In the positive direction of p_T; 2: Near the edges of the Seed	/
2	Seed	1: In the negative direction of p_T; 2: Near the edges of the Seed	/
3	Seed	1: In the positive direction of p_T; 2: Near the corner of the Seed	/
4	Seed	1: In the negative direction of p_T; 2: Near the corner of the Seed	/
5	Seed	Near the corner closest to the direction of p_T of the Seed	/
6	Cell	/	In the positive direction of p_T
7	Cell	/	In the negative direction of p_T

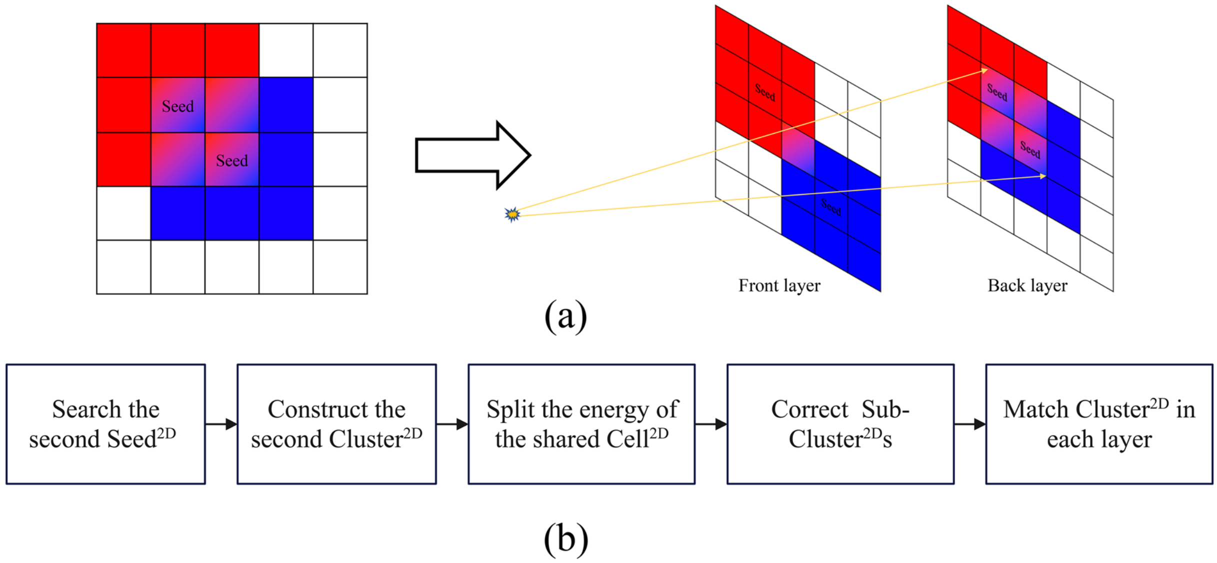

Fig. 5 (Color online) **a** A possible Cell^{3D}s response and Cell^{2D}s response in each layer of a longitudinal segmented ECAL of a merged π^0. **b** Reconstruction flow chart for merged π^0

involves a two-step process for identifying the second Seed^{2D} to enhance the accuracy of splitting Cluster^{2D} and ultimately improve the efficiency of π^0 reconstruction.

The first step is to search for Cell^{2D}, except for Seed^{2D}, which has the highest energy E' in Cluster^{2D} as Cell$^{2D'}$. The definition of E' is given by the following equation:

$$E' = \frac{E(\mathrm{Cell}^{2D})}{Frc}, \tag{5}$$

where Frc is the estimated ratio of Cell^{2D} obtained from the relationship shown in Fig. 4b. The second step is to determine whether there is any local energy maximum Cell^{2D} other than Seed^{2D} in the neighboring Cell^{2D}s of Cell$^{2D'}$ determined in the first step. If, then Cell^{2D} with this local energy maximum is taken as the second Seed^{2D}; otherwise, Cell$^{2D'}$ is taken as the second Seed^{2D}. Subsequently, the second Seed^{2D} is used to construct a new Cluster^{2D} and energy splitting for the shared Cell^{2D} and correction for Cluster^{2D} are performed as detailed in the previous sections.

3.3.2 Cluster^{2D} matching

After completing the preliminary algorithm, a sub-Cluster^{2D} pair was obtained for each layer. The algorithm described in this section aims to match the sub-Cluster^{2D}s in different layers and finally obtain two sub-Cluster^{3D}s. The subCluster^{3D} pair is regarded as a photon generated by the merged π^0. The matching of Cluster^{2D} on different layers directly affects the accuracy of the reconstruction of the final sub-Cluster^{3D}. The utilization of multidimensional information from different readout layers facilitates a more accurate Cluster^{2D} matching.

First, the energy of the sub-Cluster^{2D}s in each layer was used for prematching. Because the ratio of the deposition energy in each layer is related to the energy of the incident particles[25], unreasonable matches can be filtered based on the energy ratios between Cluster^{2D}s and the energy of Cluster^{3D} as shown in Fig. 2b. For example, in the case of a dual-layer ECAL, the energy of the Cluster^{2D}s in the front layer is used to calculate the energy of the Cluster^{2D}s in the other layers, and if the energy of the Cluster^{2D}s in the other layers exceeds the calculated value by 3σ, the prematching is considered a failure, and the matching result is filtered.

If there is more than one Cluster^{2D} in a certain layer that is prematched with the front layer, the final match is made based on the positional relationship. First, Cluster^{2D} in the front layer is connected to the initial vertex (typically, the zero point). The connection line is extended and projected onto these layers, and the closest prematched Cluster^{2D}s to the projection point are matched with the front layer Cluster^{2D} to complete the matching and obtain sub-Cluster^{3D}.

Finally, to avoid the resolution of π^0 being reconstructed in a merged model, Seed^{2D}s in all layers of sub-Cluster^{3D} must be checked to determine whether they are included in the direct reconstruction Cluster^{3D}. If so, the current process of the merged π^0 reconstruction is terminated, and a new process starts by skipping the next directly reconstructed Cluster^{3D}.

4 Performance

In the context of the LHCb experiment, a Phase-II upgrade (LHCb Upgrade II) was proposed [39]. Scheduled for installation at the beginning of LHC Run 5 around 2036, the LHCb Upgrade II aims to enhance the experimental capabilities for exploring the frontiers of particle physics. PicoCal was designed with a longitudinally layered ECAL structure. The Shashlik calorimeter structure [40, 41] was retained in the outer region of PicoCal, whereas the Spaghetti calorimeter (SpaCal) [42, 43] was used in the central region. The GAGG crystal, which is known for its high radiation resistance, high light yield, and excellent time-response performance [44–49], was introduced as a sensitive material in the most central region with the highest radiation dose. Reduced detector occupancy can be achieved by designing and using modules with smaller Molière radii to achieve smaller readout cell sizes in the internal regions with the highest detector occupancies. The detailed layout is presented in Table 2.

In this section, based on the above layout, a series of single-photon and π^0 samples are used to demonstrate the performance of the layer-reconstruction algorithm in this framework. In addition, the unlayered-reconstruction algorithm [35] employed in Run 1/2 of LHCb was introduced for comparison. To ensure fairness, the unlayered-reconstruction algorithm remained consistent with the layered reconstruction algorithm in terms of cluster correction, overlapping cluster splitting, and other steps, except for the utilization of layered information.

4.1 Single-photon performance

The single-photon samples utilized in this section were generated and simulated using the "Hybrid MC" simulation framework [50], which is built upon the GEANT4 Monte Carlo package [51]. The performance of the layered reconstruction algorithm in this framework was demonstrated in terms of the energy, position, and time resolution.

4.1.1 Energy resolution

Figure 6a illustrates the energy resolution versus the incident energy. This relationship can be described by the following equation:

$$\sigma(E)/E = \frac{a}{\sqrt{E}} \oplus b, \tag{6}$$

where a represents the statistical fluctuations of the readout signal (e.g., photoelectrons), b represents the constant term errors owing to uncertainties in the calibration and correction, as well as inhomogeneities in the active material, and $\oplus$ represents the sum of squares. The energy resolution and bias as functions of energy illustrate the stability of the layered reconstruction framework. In addition, as shown in Fig. 7, the layered reconstruction algorithm demonstrates a better energy resolution for particles with large incident angles. However, because of the forward detector design and layout of PicoCal [33], there are fewer single-photon events with large incident angles. Therefore, this improvement was not significantly reflected in the energy resolution as a function of the incident particle energy.

4.1.2 Position resolution

The position resolution is a critical parameter of the ECAL and is, to some extent, equivalent to the angular resolution. The positional resolutions are shown in Fig. 6b and d, respectively, where *Front* and *Back* represent the front and back layers, respectively, r represents the position. The development stages of the shower and readout layers change as the particles undergo showering and deposit energy along their momentum direction. However, the tendency of the reconstructed Cluster^{2D}'s raw position, relative to the true position, varied between the different layers. Essentially, if we only have the energy-weighted position information of Cell^{2D}s located in different layers, the raw position will spread out in the transverse plane owing to different tendencies. Consequently, utilizing an unlayered-reconstruction algorithm and an overall correction parameter for reconstructing the transverse position will lead to degradation of the position resolution owing to this spreading effect. In contrast, the reconstruction in this study effectively resolved the previously mentioned issue and improved the positional resolution, as illustrated in Fig. 6d. This enhancement results in an improvement of approximately 0.5 mm in the high-energy region, representing a 33% increase compared with the unlayered-reconstruction algorithm.

4.1.3 Time resolution

Time is essential for event reconstruction and data analysis in high-luminosity environments. Within the layered reconstruction framework, time information can be provided in the form of Cluster^{3D} or along the longitudinal direction using Cluster^{2D}, as shown in Fig. 6c. The integration of layered time information provides new analytical perspectives for future physical investigations. Ongoing research also focuses on exploring the application of time information for reconstruction, correction, and analysis.

4.2 π^0 reconstruction performance

In this section, approximately 30,000 signal π^0 events from $B^0 \to \pi^+\pi^-\pi^0$ are generated by the generation part of

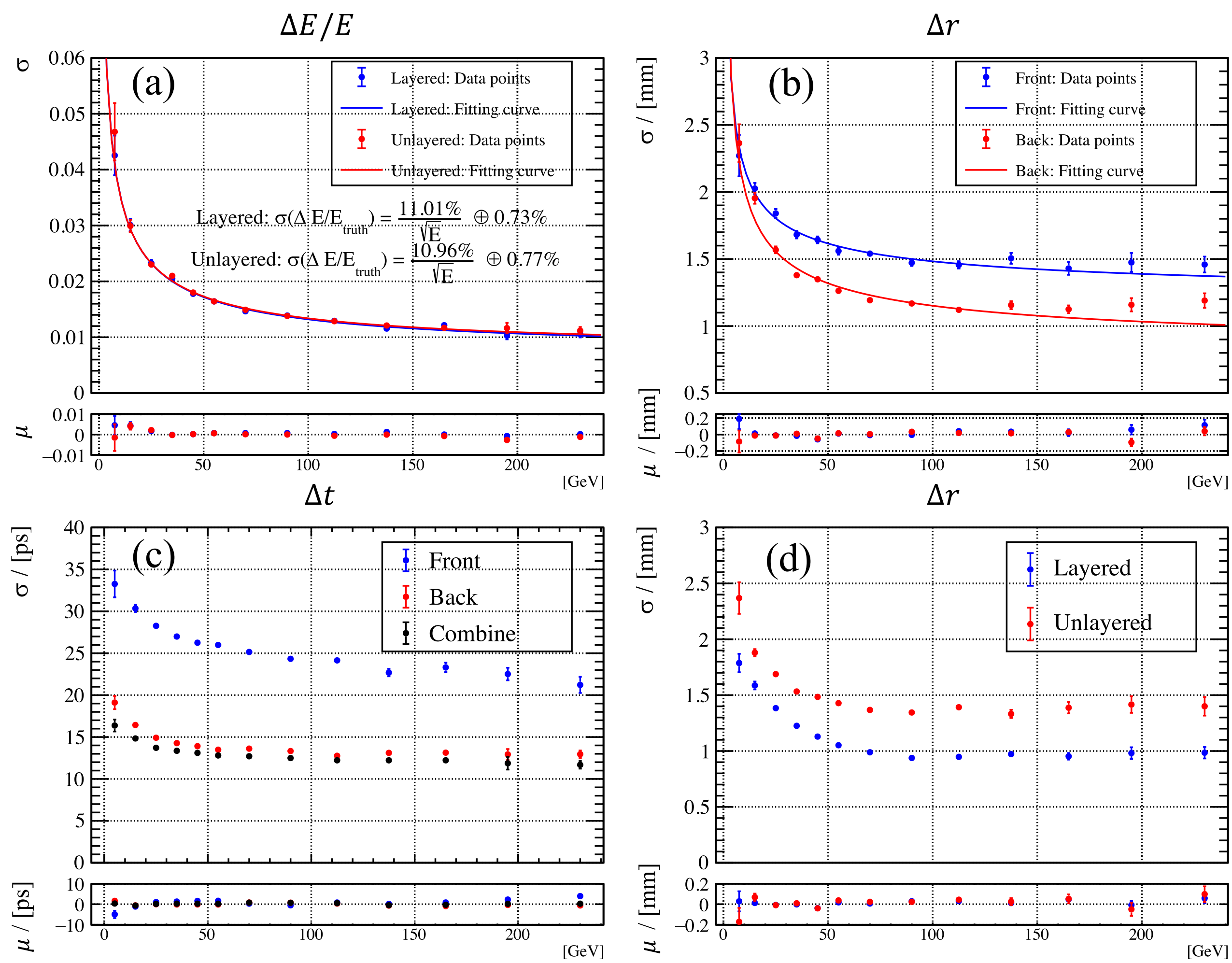

Fig. 6 (Color online) The resolution and bias relative to the true value in regions 4–7. σ and μ are derived from the Gaussian fitting, where σ represents the standard deviation (used to denote the resolution) and μ is the mean value (used to denote the bias). **a** The energy resolution and bias, where ΔE is the difference between the true energy and the reconstructed energy, and E is the true energy. **b** The position resolution and bias of front and back layers, where Δr is the difference between the true position and the reconstructed position. **c** The time resolution and bias, where Δt is the difference between the true time and the reconstructed time. **d** The position resolution and bias, where Δr is the difference between the true position and the reconstructed position

Gauss [52], with the requirement that all final-state photons from π^0 should be contained within the acceptance region of the ECAL. The transverse momentum distribution of π^0 is shown in Fig. 8a. These samples were used as benchmarks to test the contribution of the layered reconstruction algorithm in this framework to the reconstruction performance of π^0 particles. The matched $M(\gamma\gamma)$ distribution, which was compared with the unlayered-reconstruction algorithm, is shown in Fig. 8b and c. The reconstruction efficiency of π^0 based on the layered reconstruction framework is shown in Fig. 8f. An efficiency comparison of the layered and unlayered-reconstruction algorithms is presented in Fig. 8d and e, where the resolved and merged modes are presented separately.

As shown in Fig. 8d, as expected, utilizing the layered reconstruction algorithm in this framework improves the ability to split overlapping Cluster^{3D} s, leading to a 10% increase in the efficiency of reconstructing the merged π^0. The improvement in the position resolution of a single photon contributes to the improvement in the resolution of π^0 mass distribution, as shown in Fig. 8b and c.

5 Computation

This framework allows task splitting according to events, thereby enabling the deployment of different events as separate tasks. Based on this framework, we evaluated the runtime of Cluster^{3D} reconstruction under LHCb PicoCal at a center-of-mass energy of 14 TeV and an instantaneous luminosity of 1.5×10^{34} cm^{-2}s^{-1}.

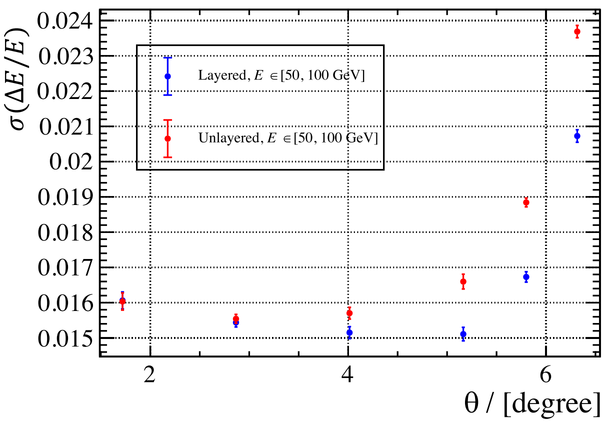

Fig. 7 (Color online) The energy resolution versus angle θ in regions 4–7. Here, θ is the angle between the particle motion direction and beam direction. ΔE represents the difference between the true and reconstructed energies, and E represents the true energy. σ is the standard deviation derived from the Gaussian fitting

The framework was deployed on a cluster CPU with an Intel(R) Xeon(R) Platinum 9242 CPU @ 2.30 GHz for each task. Because events are independent of each other in this framework, we considered only the time required for the reconstruction of each individual event. For comparison, we also introduced the unlayered-reconstruction algorithm used in LHCb, and the results are shown in Fig. 9. Compared with the unlayered-reconstruction algorithm, the layered reconstruction algorithm did not significantly increase the computation time.

Scalability is a critical consideration for CPU cluster design. In this framework, an event is defined as the smallest unit of a cluster task. This approach facilitated efficient task management and resource allocation. By increasing the number of computing nodes, the number of events processed in parallel can be increased, thereby reducing the overall task runtime. The computational speed of event reconstruction can be enhanced by using more powerful CPUs in each computing node.

The time complexity of each step in the reconstruction process for each event is shown in the flowchart in Fig. 2 and is listed in Table 3. Here, n_1 represents the number of Cell^{2D}s, n_2 represents the number of Cell^{3D}s, n_3 represents the number of Seed^{3D}s, and n_4 represents the number of Cluster^{3D}s. Considering the parallelism within an event, the structure of these processes in this framework was designed for future deployment on nodes with parallel computing capabilities, such as GPUs or FPGAs. This establishes a solid foundation for the future deployment and acceleration of these algorithms in GPU clusters and FPGA platforms.

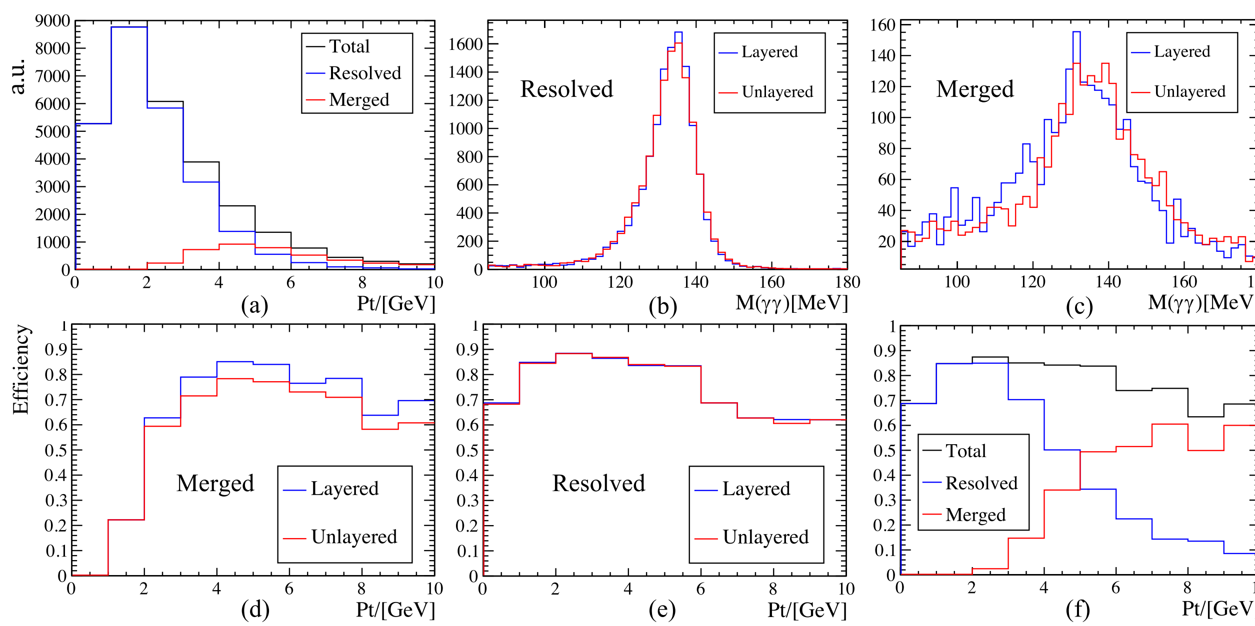

Fig. 8 (Color online) **a** The transverse momentum distribution of π^0 from $B^0 \to \pi^+\pi^-\pi^0$. **b** The distribution of $M(\gamma\gamma)$ of matched candidates in the resolved model in the SpaCal region. **c** The distribution of $M(\gamma\gamma)$ of matched candidates in the merged model in the SpaCal region. **d** The reconstruction efficiency of merged π^0 from $B^0 \to \pi^+\pi^-\pi^0$. **e** The reconstruction efficiency of resolved π^0 from $B^0 \to \pi^+\pi^-\pi^0$. **f** The total reconstruction efficiency of π^0 from $B^0 \to \pi^+\pi^-\pi^0$ in layered reconstruction framework

Table 2 Modules in 2023 baseline setup of PicoCal

Region	Type	Absorber/Crystal	Cell size (cm^2)	R_M (mm)	Layers
1	Shashlik	Lead/Polystyrene	12×12	35.0	2
2	Shashlik	Lead/Polystyrene	6×6	35.0	2
3	Shashlik	Lead/Polystyrene	4×4	35.0	2
4–7	SpaCal	Lead/Polystyrene	3×3	29.5	2
8–11	SpaCal	Tungsten/GAGG	1.5×1.5	14.5	2

Table 3 The time complexity

Algorithm	Time complexity
Construct Cell^{3D}s	$O(n_1)$
Search Seed^{3D}s	$O(n_2)$
Construct Cluster^{3D}s	$O(n_3)$
Split overlapping Cluster^{3D}s	$O(n_4^2)$
Search Seed^{2D}s/Construct Cluster^{2D}s	$O(n_4)$
Correct Cluster^{3D}s	$O(n_4)$

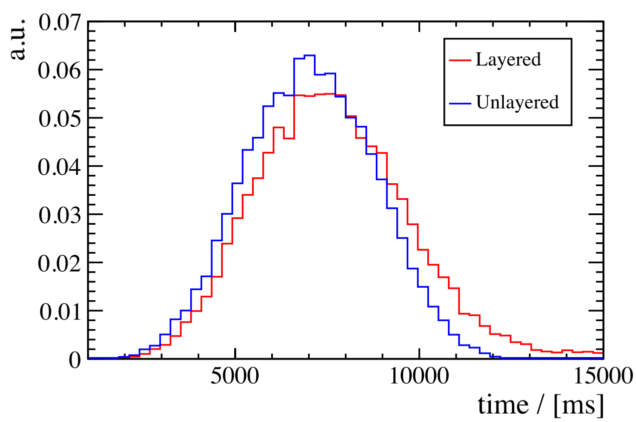

Fig. 9 (Color online) The time consumption distribution for each event

6 Conclusion

As depicted in Fig. 1, this work has accomplished we developed a software framework for the longitudinally segmented ECAL event reconstruction. Moreover, a layered reconstruction algorithm was devised within this framework for Cluster^{3D}s and the merged π^0. This framework not only furnishes the general direction, arrival time, and energy of the particle candidates in the Cluster^{3D} format, but also provides the position, timestamp, and energy deposition in each layer in the Cluster^{2D} format. The information from the Cluster^{2D}s can not only be used to filter out unreasonable Cluster^{3D}s during reconstruction, but also to provide new perspectives in physics analysis.

To achieve a more refined correction of the Cluster^{3D} information, this study leveraged the advantages of a layered reconstruction framework to provide layered information and designed a layered correction method and process. In terms of energy correction, compared with solely using the Cluster^{3D} energy for correction, this study further utilized the energy ratios of Cluster^{2D} in each layer for correction, aiming to better compensate for the longitudinal variation in the sampling fraction of the ECAL. To correct the time and position information, we first corrected the corresponding information of the Cluster^{2D}s and then weighted the corrected Cluster^{2D} information based on the resolution of the corresponding information in each layer. The weighted result was used as the corrected information for Cluster^{3D}. Moreover, this study delves into the transverse shower profile and systematically elucidates the relationship between the distance and energy ratio between Cell^{2D} s and Cluster^{2D}. This information provides more precise prior knowledge for splitting overlapping Cluster^{3D}s.

Finally, the performance of the framework was validated using the PicoCal in LHCb Upgrade II. The results show that the layered reconstruction algorithm in this framework significantly improves the position resolution of a single photon, and the energy resolution of the particles at large incident angles compared with the unlayered-reconstruction algorithm. For example, in regions 4–7 of the specified setup, the position resolution was enhanced from approximately 1.4 mm to 0.9 mm in the high-energy region. In addition, the energy resolution was improved by approximately 10% at large incident angles. Furthermore, the layered reconstruction algorithm enhances the splitting capability of overlapping clusters, leading to further improvements in the efficiency of merged π^0 reconstruction. The current version of the algorithm can increase the reconstruction efficiency of the merged π^0 by approximately 10% for SpaCal in the aforementioned setup.

Furthermore, this study provided a suitable software platform for future studies on layered ECAL. It incorporates comprehensive data structures and application programming interfaces (APIs), along with straightforward configuration and execution. This feature allows convenient secondary development by leveraging the framework to substitute and validate new algorithms. This also facilitates the investigation of ECAL-related physics. In future work, we will continue to explore various facets by utilizing the multidimensional information and scalability provided by the proposed software framework. This includes delving into the application of deep learning in cluster splitting and information correction, evaluating the performance of different cluster shapes, and scrutinizing the application of time information in cluster reconstruction.

Acknowledgements We express our gratitude to Marco Pizzichemi, Loris Martinazzoli, and Philipp Gerhard Roloff of LHCb ECAL Upgrade II R&D group for developing the simulation software and for their helpful suggestions. Additionally, we extend our thanks to the developers and maintainers of the Gauss software in LHCb, which we used to generate events. The numerical calculations in this study were performed using a supercomputing system at the Supercomputing Center of Wuhan University.

Author contributions All authors contributed to the study conception and design. Material preparation, data collection and analysis were performed by Jia-Le Fei, Ao Yuan, Ke Wei, Liang Sun and Ji-Ke Wang. The first draft of the manuscript was written by Jia-Le Fei, and all authors commented on previous versions of the manuscript. All authors read and approved the final manuscript.

Data availability The data that support the findings of this study are openly available in Science Data Bank at https://cstr.cn/31253.11.sciencedb.23305 and https://doi.org/10.57760/sciencedb.23305.

Declarations

Conflict of interest The authors declare that they have no conflict of interest.

References

1. X.Z. Yu, X.Y. Wang, W.H. Ma et al., Production and test of sPHENIX W/SciFiber electromagnetic calorimeter blocks in China. Nucl. Sci. Tech. **35**, 145 (2024). https://doi.org/10.1007/s41365-024-01517-y
2. J.Y. Zhu, Y.Z. Su, H.B. Yang et al., Design and prototyping of the readout electronics for the transition radiation detector in the high energy cosmic radiation detection facility. Nucl. Sci. Tech. **35**, 82 (2024). https://doi.org/10.1007/s41365-024-01446-w
3. J. Zhu, X.Y. Peng, S.Y. Luo, W.C. Xiao et al., Performance of the electromagnetic calorimeter module in the NICA-MPD based on Geant4. Nuclear Techniques (in Chinese) **46**, 120202 (2023). https://doi.org/10.11889/j.0253-3219.2023.hjs.46.120202
4. S. Acharya et al., Performance of the ALICE electromagnetic calorimeter. J. Instrum. **18**, P08007 (2023). https://doi.org/10.1088/1748-0221/18/08/P08007
5. R. Lindner, LHCb particle identification enhancement technical design report. CERN, Technical Report No. CERN-LHCC-2023-005, LHCB-TDR-024, Geneva (2023). https://doi.org/10.17181/CERN.LAZM.F5OH. https://cds.cern.ch/record/2866493
6. T. Boettcher, Direct photon production at LHCb. Nucl. Phys. A **982**, 251–254 (2019). https://doi.org/10.1016/j.nuclphysa.2018.10.046https://www.sciencedirect.com/science/article/pii/S0375947418303270
7. The LHCb Collaboration, LHCb detector performance. Inter. J. Modern Phys. A **30**, 1530022 (2015). https://doi.org/10.1142/S0217751X15300227
8. C. Abellán Beteta, A. Alfonso Albero, Y. Amhis et al., Calibration and performance of the LHCb calorimeters in Run 1 and 2 at the LHC. 2020, Report Number: LHCb-DP-2020-001. https://cds.cern.ch/record/2729028
9. The LHCb Collaboration, Observation of photon polarization in the $b \to s\gamma$ transition. Phys. Rev. Lett. **112**(16), 161801 (2014). https://doi.org/10.1103/PhysRevLett.112.161801
10. The LHCb Collaboration, First experimental study of photon polarization in radiative B_s^0 decays. Phys. Rev. Lett. **118**, 021801 (2017). https://doi.org/10.1103/PhysRevLett.118.021801
11. The LHCb Collaboration, Measurement of *CP* Violation in the Decay $B^+ \to K^+\pi^0$. Phys. Rev. Lett. **126**, 091802 (2021). https://doi.org/10.1103/PhysRevLett.126.091802
12. The LHCb Collaboration, Search for time-dependent *CP* violation in $D^0 \to \pi^+\pi^-\pi^0$ decays. Phys. Rev. Lett. **133**, 101803 (2024). https://doi.org/10.1103/PhysRevLett.133.101803
13. The LHCb Collaboration, Test of Lepton Universality with $B^0 \to K^0_*\ell^+\ell^-$ Decays. J. High Energ. Phys. **2017**, 55 (2017). https://doi.org/10.1007/JHEP08(2017)055
14. The LHCb Collaboration, Test of lepton universality in $b \to s\ell^+\ell^-$ decays. Phys. Rev. Lett. **131**, 051803 (2023). https://doi.org/10.1103/PhysRevLett.131.051803
15. The LHCb Collaboration, Search for the $B_s^0 \to \mu^+\mu^-\gamma$ decay. J. High Energ. Phys. **2024**, 101 (2024). https://doi.org/10.1007/JHEP07(2024)101
16. The LHCb Collaboration, Expression of interest for a Phase-II LHCb upgrade: Opportunities in flavour physics, and beyond, in the HL-LHC era. CERN Technical Report, CERN-LHCC-2017-003, Geneva (2017). https://cds.cern.ch/record/2244311
17. The LHCb Collaboration, Framework TDR for the LHCb Upgrade II: Opportunities in flavour physics, and beyond, in the HL-LHC era. CERN, Technical Report No. CERN-LHCC-2021-012, LHCB-TDR-023, Geneva (2021). https://cds.cern.ch/record/2776420
18. The LHCb Collaboration, Physics case for an LHCb Upgrade II - Opportunities in flavour physics, and beyond, in the HL-LHC era. CERN, Technical Report No. LHCB-PUB-2018-009, CERN-LHCC-2018-027, LHCC-G-171, Geneva (2016). https://doi.org/10.17181/CERN.QZRZ.R4S6. https://cds.cern.ch/record/2636441
19. I. Efthymiopoulos et al., LHCb Upgrades and operation at 10^{34} cm^{-2}s^{-1} luminosity - A first study. (2018). https://cds.cern.ch/record/2319258
20. L.M. Huhta, Physics program and performance of the ALICE Forward Calorimeter upgrade (FoCal). Proceedings of the 31st International Workshop on Deep Inelastic Scattering (DIS2024). (2024). https://cds.cern.ch/record/2910362
21. F. Orlandi, Upgrade of the CMS Barrel Electromagnetic Calorimeter for the LHC Phase-2. CERN, report number CMS-CR-2024-133, Geneva (2024). https://cds.cern.ch/record/2908787
22. The ATLAS Collaboration, Technical design report: A high-granularity timing detector for the ATLAS Phase-II Upgrade. CERN, ATLAS-TDR-031. Geneva (2020). https://cds.cern.ch/record/2719855
23. Q.Y. Shou, Y.G. Ma, S. Zhang et al., Properties of QCD matter: a review of selected results from ALICE experiment. Nucl. Sci. Tech. **35**, 219 (2024). https://doi.org/10.1007/s41365-024-01583-2
24. J.H. Chen, X. Dong, X.H. He et al., Properties of the QCD matter: review of selected results from the relativistic heavy ion collider beam energy scan (RHIC BES) program. Nucl. Sci. Tech. **35**, 214 (2024). https://doi.org/10.1007/s41365-024-01591-2
25. M. Livan, R. Wigmans, Calorimetry for Collider Physics, an Introduction, 1st ed. (2019). http://lib.ugent.be/catalog/ebk01:4100000008707558
26. The CMS Collaboration, Performance of electron reconstruction and selection with the CMS detector in proton-proton collisions at $\sqrt{s} = 8$ TeV. J. Instrum. **10**, P06005 (2015). https://doi.org/10.

1088/1748-0221/10/06/P06005.https://cds.cern.ch/record/1988091

27. The CMS Collaboration, Electron and photon reconstruction and identification with the CMS experiment at the CERN LHC. J. Instrum. **16**, P05014 (2021). https://doi.org/10.1088/1748-0221/16/05/P05014.https://cds.cern.ch/record/2747266
28. The CMS Collaboration, Performance of photon reconstruction and identification with the CMS detector in proton-proton collisions at $\sqrt{s}$= 8 TeV. J. Instrum. **10**, P08010 (2015)
29. S. Nair, Simulation studies of π^0, η and ω meson reconstruction performance in pp collisions at $\sqrt{s}$ = 14 TeV in Forward Calorimeter (FoCal). Indian Inst. Tech. Indore, 2023. https://cds.cern.ch/record/2860262
30. M. rovere, ZH. Chen, A. Di Pilato et al., CLUE: a fast parallel clustering algorithm for high granularity calorimeters in high-energy physics. Front. Big Data **3**, 591315 (2020). https://doi.org/10.3389/fdata.2020.591315
31. F. pantaleo, M. rovere, The iterative clustering framework for the CMS HGCAL reconstruction. J. Phys. Conf. Ser. **2438**, 012096 (2023). https://doi.org/10.1088/1742-6596/2438/1/012096
32. Sergei Kholodenko, LHCb ECAL UII working group, LHCb ECAL upgrade II. PoS **PANIC2021**, 100 (2022). https://doi.org/10.22323/1.380.0100. https://cds.cern.ch/record/2836693
33. The LHCb Collaboration, LHCb Upgrade II scoping document. CERN. CERN-LHCC-2024-010, LHCB-TDR-026. Geneva (2024). https://cds.cern.ch/record/2903094
34. V. Breton, N. Brun, P. Perret, A clustering algorithm for the LHCb electromagnetic calorimeter using a cellular automaton. CERN. LHCb-2001-123. Geneva (2001). https://cds.cern.ch/record/681262
35. O. Deschamps, F.P. Machefert, M.H. Schune et al., Photon and neutral pion reconstruction. CERN-LHCb-2003-091 (2003)
36. C. Grupen, B. Shwartz, *Particle Detectors*, 2nd edn. Nuclear Physics and Cosmology (Cambridge University Press, Cambridge, Cambridge Monographs on Particle Physics, 2008)
37. F. P. Machefert, P. Robbe, M. H. Schune et al., $B^0 \to \pi^+\pi^-\pi^0$ reconstruction with the re-optimized LHCb detector. CERN, Technical Report No. LHCb-2003-077, Geneva (2003). https://cds.cern.ch/record/691636
38. H. Terrier, I. Belyaev, Particle identification with LHCb calorimeters. CERN (2003). https://cds.cern.ch/record/691743
39. The LHCb Collaboration, The LHCb Detector at the LHC. J. Instrum. **3**, S08005 (2008). https://doi.org/10.1088/1748-0221/3/08/S08005
40. S. Barsuk, A. Golutvin, V. Kochetkov et al., Design and construction of electromagnetic calorimeter for LHCb experiment. CERN Technical Report, LHCb-2000-043, Geneva (2000). https://cds.cern.ch/record/691508
41. The LHCb Collaboration, LHCb calorimeters: Technical Design Report. CERN, Technical Design Report. LHCb, Geneva (2000). https://cds.cern.ch/record/494264
42. P. Jenni, P. Sonderegger, H.P. Paar et al., The high resolution spaghetti hadron calorimeter: proposal. CERN Technical Report, NIKHEF-H-87-7, Geneva (1987). https://cds.cern.ch/record/181281
43. L. An, E. Auffray, F. Betti et al., Performance of a spaghetti calorimeter prototype with tungsten absorber and garnet crystal fibres. Nucl. Instrum. Methods Phys. Res. A **1045**, 167629 (2023). https://doi.org/10.1016/j.nima.2022.167629.https://www.sciencedirect.com/science/article/pii/S0168900222009214
44. V. Alenkov, O. Buzanov, G. Dosovitskiy et al., Irradiation studies of a multi-doped $Gd_3Al_2Ga_3O_{12}$ scintillator. Nucl. Instrum. Methods Phys. Res. A **916**, 226–229 (2019). https://doi.org/10.1016/j.nima.2018.11.101
45. K. Kamada, T. Endo, K. Tsutumi et al., Composition engineering in cerium-doped $(Lu,Gd)_3(Ga,Al)_5O_{12}$ single-crystal scintillators. Cryst. Growth Des. **11**, 4484–4490 (2011). https://doi.org/10.1021/cg200694a
46. M. Nikl, K. Kamada, V. Babin et al., Defect engineering in Ce-doped aluminum garnet single crystal scintillators. Cryst. Growth Des. **14**, 4827–4833 (2014). https://doi.org/10.1021/cg501005s
47. M.T. Lucchini, V. Babin, P. Bohacek et al., Effect of Mg^{2+} ions co-doping on timing performance and radiation tolerance of Cerium doped $Gd_3Al_2Ga_3O_{12}$ crystals. Nucl. Instrum. Meth. Phys. Res. Sect. A **816**, 176–183 (2016). https://doi.org/10.1016/j.nima.2016.02.004
48. L. Martinazzoli, N. Kratochwil, S. Gundacker et al., Scintillation properties and timing performance of state-of-the-art $Gd_3Al_2Ga_3O_{12}$ single crystals. Nucl. Instrum. Meth. Phys. Res. Sect. A. **1000**, 165231 (2021). https://doi.org/10.1016/j.nima.2021.165231
49. M.T. Lucchini, K. Pauwels, K. Blazek et al., Radiation tolerance of LuAG: Ce and YAG: Ce crystals under high levels of gamma- and proton-irradiation. IEEE Trans. Nucl. Sci. **63**, 586–590 (2016). https://doi.org/10.1109/TNS.2015.2493347
50. M. Pizzichemi, L. Martinazzoli, Hybrid-MC. (2024). https://gitlab.cern.ch/spacal-rd/spacal-simulation
51. S. Agostinelli, J. Allison, K. Amako et al., Geant4-a simulation toolkit. Nucl. Instrum. Meth. Phys. Res. Sect. A **506**, 250–303 (2003). https://doi.org/10.1016/S0168-9002(03)01368-8
52. The LHCb Collaboration, The LHCb simulation application, Gauss: design, evolution and experience. J. Phys. **331**, 032023 (2011). https://doi.org/10.1088/1742-6596/331/3/032023